

Actions, angles and frequencies for numerically integrated orbits

Jason L. Sanders* & James Binney

Rudolf Peierls Centre for Theoretical Physics, Keble Road, Oxford, OX1 3NP, UK

14 June 2018

ABSTRACT

We present a method for extracting actions, angles and frequencies from an orbit’s time series. The method recovers the generating function that maps an analytic phase-space torus to the torus to which the orbit is confined by simultaneously solving the constraints provided by each time step. We test the method by recovering the actions and frequencies of tori in a triaxial Stäckel potential, and use it to investigate the structure of orbits in a triaxial potential that has been fitted to our Galaxy’s Sagittarius stream. The method promises to be useful for analysing N -body simulations. It also takes a step towards constructing distribution functions for the triaxial components of our Galaxy, such as the bar and dark halo.

Key words: methods: numerical – Galaxy: kinematics and dynamics – galaxies: kinematics and dynamics

1 INTRODUCTION

Although no galaxy is ever in perfect dynamical equilibrium, equilibrium dynamical models are central to the interpretation of observations of both our Galaxy and external galaxies. A major reason for the importance of equilibrium models is that we can infer a galaxy’s gravitational potential, and thus its dark-matter distribution, only to the extent that the galaxy is in equilibrium. Moreover, equilibrium models are the simplest models and more complex configurations, involving spiral structure or an on-going minor merger for example, are best modelled as perturbations of an equilibrium model.

Globular clusters are the stellar systems that are most completely understood, and the theory of these systems illustrates the importance of equilibrium models: at each instant the cluster is assumed to be in dynamical equilibrium, so, by Jeans’ theorem, its distribution function (DF) is a function of the relevant isolating integrals, such as stellar energy E , total angular momentum L , or angular momentum about a symmetry axis, L_z . Over many dynamical times encounters between stars and stellar evolution cause the DF to change, but in such a way that the DF continues to satisfy Jeans’ theorem, so the cluster evolves through a series of dynamical equilibria.

N -body simulations of cosmological clustering likewise yield a picture in which dark-matter haloes are far from dynamical equilibrium only during short-lived and quite rare major mergers. In general a dark-matter halo can be well approximated by a dynamical equilibrium that is mildly perturbed by accretion.

The natural way to model a dynamical equilibrium is via Jeans theorem, which assures us that the system’s DF can be assumed to be a non-negative function of isolating integrals. Since one expects a smooth time-independent gravitational potential to admit up

to three functionally independent isolating integrals, Jeans theorem states that we should be able to represent an equilibrium stellar system by the density of stars in a three-dimensional space of integrals rather than in full six-dimensional phase space. This reduction in dimensionality makes the system very much easier to comprehend and model.

Since any function of integrals is itself an integral, infinitely many different integrals may be used as arguments of the DF. However, the action integrals J_i stand out as uniquely suited to be used as arguments of the DF. What makes actions special is that they can be complemented by canonically conjugate variables, the angles θ_i , to form a complete set of canonical phase-space coordinates. Obviously the equations of motion of the actions are trivial: $\dot{J}_i = 0$. More remarkably the equations of motion of the angles are almost as trivial: $\dot{\theta}_i = \Omega_i(\mathbf{J}) = \text{constant}$. Thus the angle variables increase linearly in time and if we use angle-action coordinates, the unperturbed motion of stars becomes trivial. This fact makes angle-action coordinates uniquely suited to work involving perturbation theory, and indeed the angle-action coordinates of the Kepler problem were invented to explore the role played by planet-planet interactions in the dynamics of the Solar System.

McMillan & Binney (2008) have shown that angle-action coordinates make it possible to identify stars near the Sun that have been stripped from an object that was tidally disrupted gigayears ago, and even to determine the date of the disruption to good precision. Sellwood (2010) and McMillan (2013) have used angle-action coordinates to identify stars near the Sun that are resonantly trapped by spiral structure. Sanders & Binney (2013) have shown how angle-action coordinates for the stars of a stream enable one to constrain the gravitational potential in which the stream moves.

Cosmological simulations have shown that triaxial dark matter haloes are to be expected, at least up to the point at which baryons become gravitationally dominant (Valluri et al. 2010). Moreover, Law & Majewski (2010) and Vera-Ciro & Helmi (2013) present

* E-mail: jason.sanders@physics.ox.ac.uk

evidence that the tidal tails of the Sagittarius dwarf galaxy can only be fitted if the Milky Way has a triaxial dark matter halo. Hence we need to be able to determine angle-action coordinates for stars in triaxial potentials. In this paper we show how to evaluate the angles and actions of particles in a given triaxial potential. If the potential is axisymmetric, the actions can be evaluated using the algorithm given by Binney (2012a).

In Section 2 we derive the equations that yield values of angles, frequencies and actions. In Section 3 we test our solutions of these equations by comparing the resulting angles, frequencies and actions for two orbits in a Stäckel potential with analytic values. In Section 4 we use the equations to explore a constant-energy surface of the action space of the triaxial potential for our Galaxy that Law & Majewski (2010) fitted to the tidal stream of the Sagittarius dwarf. In Section 5 we relate our work to previous work in the field, discuss a possible extension, and explore how the method copes with resonant trapping. Section 6 sums up and looks to the future.

2 FORMALISM

Angles and actions can be assigned to orbits that are “regular” or quasiperiodic because such an orbit is confined to a torus labelled by the actions (Arnold 1978). We will work in three dimensions so will have three actions denoted as $\mathbf{J} = (J_1, J_2, J_3)$. Each action quantifies the magnitude of the oscillation in a suitable coordinate.

The transformation from ordinary phase-space coordinates (\mathbf{x}, \mathbf{v}) to angle-action coordinates $(\boldsymbol{\theta}, \mathbf{J})$ is possible analytically in only a few cases. McGill & Binney (1990) used one of these cases as a starting point for the numerical construction of more general transformations by “torus mapping”. The key point about torus mapping is that it yields orbits with specified actions rather than orbits with specified initial conditions (\mathbf{x}, \mathbf{v}) . When analysing an N -body model, we require actions given an initial condition and not vice versa. Here we adapt the approach of McGill & Binney (1990) into a procedure which finds the actions, angles and frequencies given a series of phase-space coordinates $(\mathbf{x}_i, \mathbf{v}_i)$ sampled along an orbit at times t_i , where $0 \leq t_i \leq T$.

With this time series we seek a generating function that will map a “toy torus” of a simple “toy potential” into the “target torus” to which the orbit is confined. The toy potential must have analytically tractable angles and actions and permit orbits that have the correct geometry.

In the absence of figure rotation, a general triaxial potential admits two basic classes of non-resonant orbit: loop orbits and box orbits (Schwarzschild 1979; de Zeeuw 1985). Loop orbits have a definite sense of rotation either around the long- or short-axis of the potential, whilst a box orbit has no sense of rotation and can reach down to the centre of the potential. Hence the class of an orbit can be determined by inspection of components of the angular momentum along the orbit: if all components of the angular momentum change sign, the orbit has no sense of circulation and is a box orbit; when a component of the angular momentum retains its sign, the orbit is a loop orbit around the corresponding axis (Carpintero & Aguilar 1998). For each class of orbit we use a toy potential that provides tori with the same geometrical structure as the tori of the given orbit class.

For a box orbit the actions J_1 , J_2 and J_3 quantify the oscillation in the x , y and z directions, respectively. For loop orbits, J_1 quantifies oscillation in a generalized radial coordinate. For a short-axis loop J_2 quantifies the particle’s circulation around the

short axis, whilst J_3 quantifies oscillation parallel to this axis. For a long-axis loop orbit, J_3 quantifies circulation around the long axis, whilst J_2 quantifies oscillation parallel to this axis. We choose this definition such that our actions match J_λ , J_μ and J_ν for a Stäckel potential (de Zeeuw 1985), and each class of orbit occupies a distinct region of action space (see Section 4).

2.1 Toy potentials

2.1.1 Triaxial harmonic oscillator

For box orbits we use the potential of the triaxial harmonic oscillator,

$$\Phi_{\text{ho}}(\mathbf{x}) = \frac{1}{2} \sum_{i=1}^3 \omega_i^2 x_i^2, \quad (1)$$

which has three parameters, ω_i . Here we have chosen the principal axes of the potential to lie along the Cartesian x , y , z directions on the assumption that the time series has already been rotated into the coordinate system that is aligned with the principal axes of the true potential. The actions and angles in this potential are given by

$$J_i = \frac{p_i^2 + \omega_i^2 x_i^2}{2\omega_i}, \quad (2)$$

$$\theta_i = \arctan\left(\frac{p_i}{\omega_i x_i}\right).$$

2.1.2 Isochrone sphere

For loop orbits we use the isochrone potential,

$$\Phi_{\text{iso}}(\mathbf{x}) = \frac{-GM}{b + \sqrt{b^2 + r^2}}, \quad (3)$$

where r is the spherical radius. This potential has two free parameters: the mass M and the scale radius, b . The expressions for the actions and angles in this potential are more involved than for the harmonic oscillator so are not repeated here. Readers can consult Binney & Tremaine (2008) for the appropriate equations. The three actions in the isochrone potential are given by the radial action J_r , the z -component of the angular momentum L_z and the vertical action $J_z \equiv L - |L_z|$, where L is the total angular momentum. With this choice we must orient our coordinate system, such that the orbit circulates around the z -axis, before finding the actions.

2.1.3 Offsets

One might also include the offset of the centre of the potential from the coordinate centre as a free parameter, but we shall not do so here, presuming instead that the time samples x_i have already been adjusted to be relative to one’s best estimate of the centre of the true potential.

2.1.4 Parameter choice

Once a class of potential has been chosen, we set the parameters of the potential by minimizing (McGill & Binney 1990)

$$\chi^2 = \sum_i (H_i - \langle H \rangle)^2, \quad (4)$$

where the sum is over the times, H_i is the value of the toy Hamiltonian at $(\mathbf{x}_i, \mathbf{v}_i)$, and $\langle H \rangle$ is the mean of these values. The minimization of χ^2 is done using the Levenberg–Marquardt algorithm (Press et al. 2002).

The experiments described below suggest that this method for selecting the parameters is sub-optimal in that it leads to a rather centrally concentrated toy potential being selected. This central concentration then leads to high-order Fourier components being required in the generating function. However, our attempts to find a better procedure for selecting the toy potential have not met with success.

2.2 Generating Function

With a toy potential chosen, we construct the generating function to transform between the angle-actions $(\boldsymbol{\theta}, \mathbf{J})$ of the toy potential, and those $(\boldsymbol{\theta}', \mathbf{J}')$ of the target potential. The generating function for this transformation, $S(\boldsymbol{\theta}, \mathbf{J}')$, can be written

$$S(\boldsymbol{\theta}, \mathbf{J}') = \boldsymbol{\theta} \cdot \mathbf{J}' - i \sum_{\mathbf{n} \neq \mathbf{0}} S_n(\mathbf{J}') e^{i\mathbf{n} \cdot \boldsymbol{\theta}}, \quad (5)$$

where the vector \mathbf{n} has integer components. The first term on the right generates the identity transformation, whilst the structure of the second part is required by the periodicity of the angle variables.

McGill & Binney (1990) show that if the Hamiltonian is time-reversible, the reality of the generating function requires the S_n to satisfy

$$S_n = -S_{-\mathbf{n}}. \quad (6)$$

For this condition to be satisfied there must exist a point on the toy torus at which $\dot{\mathbf{J}} = \mathbf{0}$ – in Appendix A we demonstrate that this is true for the toy potentials of the previous section. With this constraint, the generating function can be written as

$$S(\mathbf{J}', \boldsymbol{\theta}) = \boldsymbol{\theta} \cdot \mathbf{J}' + 2 \sum_{\mathbf{n} \in \mathbf{N}} S_n(\mathbf{J}') \sin \mathbf{n} \cdot \boldsymbol{\theta}, \quad (7)$$

where the integer vectors \mathbf{n} are now restricted to just half of a three-dimensional lattice. We take this half to be the set $\mathbf{N} = \{(i, j, k)\}$, where either $(k > 0)$, $(k = 0, j > 0)$ or $(k = 0, j = 0, i > 0)$. Symmetries of the target potential require some of the S_n to be zero. This is discussed further in Appendix A.

From the generating function (7) we find that the toy actions are

$$\mathbf{J} = \frac{\partial S}{\partial \boldsymbol{\theta}} = \mathbf{J}' + 2 \sum_{\mathbf{n} \in \mathbf{N}} \mathbf{n} S_n(\mathbf{J}') \cos \mathbf{n} \cdot \boldsymbol{\theta}, \quad (8)$$

and the target angles are

$$\boldsymbol{\theta}' = \frac{\partial S}{\partial \mathbf{J}'} = \boldsymbol{\theta} + 2 \sum_{\mathbf{n} \in \mathbf{N}} \frac{\partial S_n}{\partial \mathbf{J}'}(\mathbf{J}') \sin \mathbf{n} \cdot \boldsymbol{\theta}. \quad (9)$$

Note that by the choice of our generating function, the target angle zero-point coincides with the toy-angle zero-point.

Given the choice of a toy Hamiltonian, we may find the toy actions and angles $(\mathbf{J}(t_i), \boldsymbol{\theta}(t_i))$ at each time. Each time then produces a separate equation (8) with common unknowns: the target actions and the Fourier components of the generating function, S_n .

We cannot solve these equations exactly because we are dealing with equations in an infinite number of unknowns. Because we can include only a finite number of terms on the right-hand side of each equation, the right-hand sides should not agree exactly with the left-hand sides, and the correct procedure is to minimize the sum of the squares of the residuals of individual equations. This sum is

$$E = \sum_i \sum_k \left(J_k(t_i) - J'_k - 2 \sum_{\mathbf{n} \in \mathbf{N}} n_k S_n(\mathbf{J}') \cos \mathbf{n} \cdot \boldsymbol{\theta}(t_i) \right)^2, \quad (10)$$

where the inner sum is over the dimension of the action space and the set \mathbf{N} is limited to a finite number of vectors \mathbf{n} . We take this set to be the N vectors that satisfy the condition $|\mathbf{n}| \leq N_{\max}$, where $N_{\max} \simeq 6$.

We minimize E by setting to zero its derivatives with respect to the unknowns:

$$\begin{aligned} 0 &= \frac{\partial E}{\partial J'_k} \\ &= -2 \sum_i \left(J_k(t_i) - J'_k - 2 \sum_{\mathbf{n} \in \mathbf{N}} n_k S_n(\mathbf{J}') \cos \mathbf{n} \cdot \boldsymbol{\theta}(t_i) \right) \\ 0 &= \frac{\partial E}{\partial S_m} \\ &= -2 \sum_i \sum_k 2m_k \cos \mathbf{m} \cdot \boldsymbol{\theta}(t_i) \\ &\quad \times \left(J_k(t_i) - J'_k - 2 \sum_{\mathbf{n} \in \mathbf{N}} n_k S_n(\mathbf{J}') \cos \mathbf{n} \cdot \boldsymbol{\theta}(t_i) \right). \end{aligned} \quad (11)$$

To solve these equations we define a matrix $\mathbf{c}_{\mathbf{n}k}$ that has as subscripts the vector \mathbf{n} and the integer $k = 1, 2, 3$ that selects a particular spatial dimension. This N -by-3 matrix is

$$\mathbf{c}_{\mathbf{n}k}(t_i) \equiv 2n_k \cos(\mathbf{n} \cdot \boldsymbol{\theta}(t_i)), \quad (\text{no sum over } \mathbf{n}). \quad (12)$$

We further define two $(3 + N)$ -vectors

$$\mathbf{x}_{\mathbf{J}} \equiv (\mathbf{J}', S_n), \quad \mathbf{b}_{\mathbf{J}} \equiv \sum_i (\mathbf{J}(t_i), \mathbf{c}_{\mathbf{n}}(t_i) \cdot \mathbf{J}(t_i)), \quad (13)$$

and the symmetric matrix

$$\mathbf{A}_{\mathbf{J}} \equiv \sum_i \begin{pmatrix} \mathbf{I}_3 & \mathbf{c}_{\mathbf{n}}^T(t_i) \\ \mathbf{c}_{\mathbf{n}}(t_i) & \mathbf{c}_{\mathbf{n}}(t_i) \cdot \mathbf{c}_{\mathbf{n}}^T(t_i) \end{pmatrix}. \quad (14)$$

Here \mathbf{I}_3 is the 3-by-3 identity matrix. With these definitions, the equations (11) to be solved can be written as

$$\mathbf{A}_{\mathbf{J}} \cdot \mathbf{x}_{\mathbf{J}} = \mathbf{b}_{\mathbf{J}}. \quad (15)$$

We solve these equations for $\mathbf{x}_{\mathbf{J}}$ by LU decomposition (Press et al. 2002).

A similar procedure yields the target angles from equation (9). We note that at time t_i the orbit has $\boldsymbol{\theta}'(t_i) = \boldsymbol{\theta}'(0) + \boldsymbol{\Omega}' t_i$ where $\boldsymbol{\Omega}'$ is the target frequency, and $\boldsymbol{\theta}'(0)$ is the angle corresponding to the initial point in the orbit integration. The relevant sum of squared residuals is

$$F = \sum_i \sum_k \left(\theta'_k(0) + \Omega'_k t_i - \theta_k(t_i) - 2 \sum_{\mathbf{n} \in \mathbf{N}} \frac{\partial S_n}{\partial J'_k}(\mathbf{J}') \sin \mathbf{n} \cdot \boldsymbol{\theta} \right)^2. \quad (16)$$

The unknowns now are $\boldsymbol{\theta}'(0)$, $\boldsymbol{\Omega}'$ and the set of $\partial S_n / \partial \mathbf{J}'$. The requirement of vanishing partial derivatives of F with respect to the unknowns yields the matrix equation,

$$\mathbf{A}_{\boldsymbol{\theta}} \cdot \mathbf{x}_{\boldsymbol{\theta}} = \mathbf{b}_{\boldsymbol{\theta}}. \quad (17)$$

These symbols are defined in Appendix B. The toy angles will be 2π -periodic, and we require the same for the target angles $\boldsymbol{\theta}'(0) + \boldsymbol{\Omega}' t_i$. However, in order to solve the matrix equation we must first make the $\boldsymbol{\theta}(t_i)$ from the orbit integration continuously increase, and then we solve for the target angles and take the 2π -modulus.

2.3 Choice of N_T , N_{\max} and T

Given the scheme presented above, the only questions that remain are how to select the orbit integration time T , the number of time samples, N_T , to use, and what value to use for N_{\max} , which determines the number N of Fourier components we solve for. Here we discuss how we can automatically choose these parameters such that we have good recovery of the unknowns.

A necessary condition is that the number of unknowns must be less than the number of time samples, N_T . For the action calculation the number of unknowns is approximately $N_{\max}^3/2$, whilst for the angle-frequency calculation we have $\sim 3N_{\max}^3/2$ unknowns. We also expect our ability to recover the unknowns to depend upon the sampling of the toy angle space.

Let us first consider an idealised 1D case. If we were able to sample uniformly in the toy angle of a 1D system, we would select N_T points in a single period separated in toy angle by $\Delta = 2\pi/N_T$. With this sampling rate we would be able to constrain all modes $e^{in\theta}$ with $n\Delta \leq \pi$. We can choose to constrain only the N_{\max} modes with $n < \pi/\Delta$ as then we would be super-sampling the highest considered modes. Here we are using a time series that is a product of an orbit integration so is not uniformly spaced in toy angles – the toy-angle distribution depends on the target Hamiltonian, the toy potential and the distribution of sampling times. The recovery of Fourier components from non-uniform samples is discussed in Marvasti (2001). To constrain modes from a 1D non-uniform sampling we must sample on average at or above the Nyquist frequency. If we have toy-angle samples θ_i we require

$$\frac{n}{N_T - 1} \sum_{i=1}^{i=N_T-1} (\theta_{i+1} - \theta_i) \leq \pi, \quad (18)$$

to constrain mode n .

Here we are attempting to recover components from samples, θ_i , in 3D toy-angle space. As we are restricted to using samples generated from an orbit integration, our sampling is limited to some sub-space of the full 3D toy-angle space. The 3D sampling can be considered as a series of 1D samples in $\mathbf{n} \cdot \boldsymbol{\theta}_i$ (we first unroll the angles such that they increase continuously). In order to recover the S_n from this toy-angle sampling we need to satisfy two conditions:

(i) As in the 1D case we need to sample on average at or above the Nyquist frequency such that

$$\frac{1}{N_T - 1} \sum_{i=1}^{i=N_T-1} \mathbf{n} \cdot (\boldsymbol{\theta}_{i+1} - \boldsymbol{\theta}_i) \leq \pi. \quad (19)$$

(ii) For every included mode, \mathbf{n} , we would also like a good total coverage in $\mathbf{n} \cdot \boldsymbol{\theta}$. We choose to require that the $\mathbf{n} \cdot \boldsymbol{\theta}$ samples cover the full range from 0 to 2π :

$$\max(\mathbf{n} \cdot \boldsymbol{\theta}) - \min(\mathbf{n} \cdot \boldsymbol{\theta}) > 2\pi. \quad (20)$$

If this condition is not satisfied, we are including a mode which will not be well constrained by the toy-angle sampling i.e. the average of $\cos \mathbf{n} \cdot \boldsymbol{\theta}$ will not be near zero. We therefore expect that the corresponding S_n will not be well recovered from this sampling. It could be that this S_n is not significant so will not affect the recovered actions and frequencies significantly. However, a conservative approach would ensure that equation (20) is satisfied for all included modes.

The second of these conditions is the stricter. To ensure that the toy-angle sampling satisfies equation (20) when an orbit is near-resonant, we require time samples which span a very large number

of periods. This is an inevitable drawback of the approach taken here because we have very little control over the sampling in the toy angle space.

Having identified a mode which will not be well constrained, one possibility is to set $S_n = 0$ for this mode. However, by doing this, we risk throwing out a mode which is significant, and the recovery of the actions and frequencies will deteriorate so we opt not to do this.

Another requirement is that the S_n (and $\partial S_n / \partial \mathbf{J}'$) decrease as we go to larger \mathbf{n} such that the truncation at N_{\max} is valid. If the S_n do not decrease with \mathbf{n} , this is evidence of aliasing such that these higher \mathbf{n} modes are not well recovered and we expect the actions, angles and frequencies will also not be well recovered.

2.3.1 Procedure

We will now summarize the above discussion into a procedure that can be implemented:

- We first select a reasonable N_{\max} , for instance $N_{\max} = 6$ is used in the later examples.
- We then integrate for some time T recording at least $N_T = 3N + 6$ time samples (or $N_T = N + 3$ if we only need the actions) such that we have as many equations as unknowns. This is always satisfied if we choose

$$N_T = \max(200, \frac{9N_{\max}^3}{4}). \quad (21)$$

- For each time sample we find the toy angles and check that equations (19) and (20) are satisfied for each mode. If equation (19) is not satisfied, T is much longer than the fundamental orbital periods and so we require a finer time sampling from the orbit integration. If equation (20) is not satisfied then we continue integrating the orbit until this equation is satisfied for all the modes.
- We then perform the procedure outlined in Section 2.2 to find the S_n . We require the S_n to be decreasing with \mathbf{n} such that on the boundaries the values of the S_n are small. If we find that the boundary values of S_n are large, we have not included a sufficient number of modes in the generating function so we must increase N_{\max} and repeat the above procedure until we are satisfied that all dominant modes are included.

As we will see below this procedure is very conservative but should ensure that the recovery of the actions, angles, frequencies and components of the generating function are accurate.

3 EXAMPLE

As a test of the above, let us look at an example. The most general separable triaxial potential is the triaxial Stäckel potential (de Zeeuw 1985). We choose to work with the perfect ellipsoid, which has density profile

$$\rho(x, y, z) = \frac{\rho_0}{(1 + m^2)^2}, \quad (22)$$

where

$$m^2 \equiv \frac{x^2}{a^2} + \frac{y^2}{b^2} + \frac{z^2}{c^2}, \quad a \geq b \geq c \geq 0. \quad (23)$$

The associated coordinates are confocal ellipsoidal coordinates in which the actions can be expressed as one-dimensional integrals. These may be calculated numerically using Gauss-Legendre quadrature. Similarly the frequencies can also be determined from

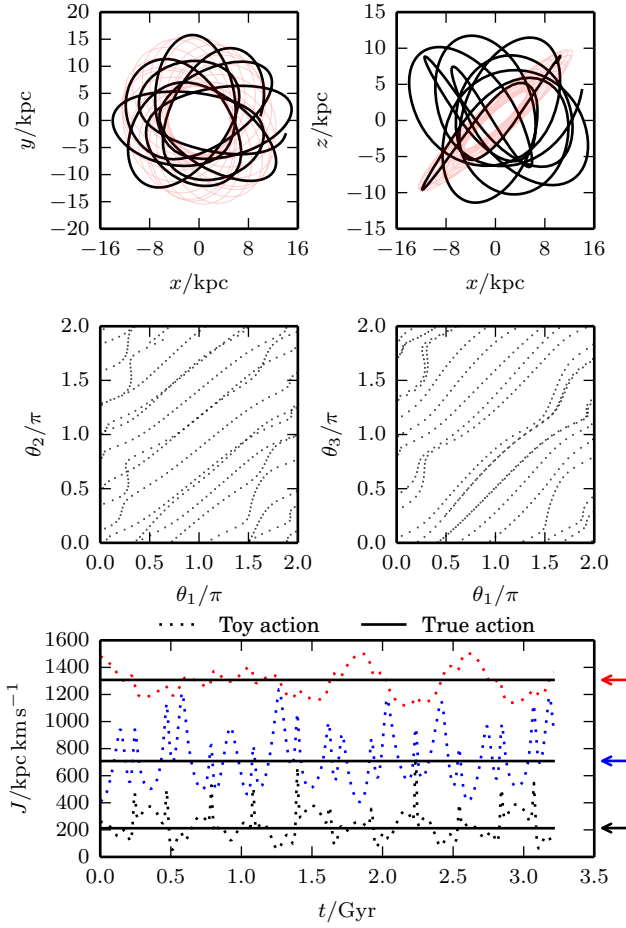


Figure 1. Example loop orbit in the triaxial Stäckel potential – the top panels shows in black the orbit integrated in the test potential. This is a short-axis loop orbit so circulates about the axis $z = 0$. In faint red we show the initial point integrated in the best-fitting isochrone potential. In the middle panels we show the toy angles calculated at each time sample. In the bottom panel we show the toy actions at each time-step as a dotted line (black for J_1 , blue for J_2 and red for J_3). The solid lines show the true actions and the arrows mark the estimated actions.

one-dimensional integrals. Equations for these quantities are given in de Zeeuw (1985). Here we work with the potential with parameters $\rho_0 = 7.2 \times 10^8 M_\odot \text{kpc}^{-3}$, $a = 5.5 \text{kpc}$, $b = 4.5 \text{kpc}$ and $c = 1 \text{kpc}$.

In this potential we examine two orbits – a short-axis loop orbit with initial condition $(x, y, z) = (10, 1, 8) \text{kpc}$, $(v_x, v_y, v_z) = (40, 152, 63) \text{km s}^{-1}$ and a box orbit with initial condition $(x, y, z) = (0.1, 0.1, 0.1) \text{kpc}$, $(v_x, v_y, v_z) = (142, 140, 251) \text{km s}^{-1}$. Each orbit was integrated for eight times the longest period, T_F . We set $N_{\text{max}} = 6$ and calculated the corresponding number of uniformly-spaced time samples required from equation (21). We ensured that equations (19) and (20) were satisfied for all the included modes. In Figs 1 and 2 we show the orbits in the (x, y) and (x, z) planes, the sampling of the toy-angle space and the resultant actions. We also show, in faint red, the result of integrating in the best-fitting toy potential. This gives us an idea of the work that the generating function has to do to deform the toy torus into the target torus.

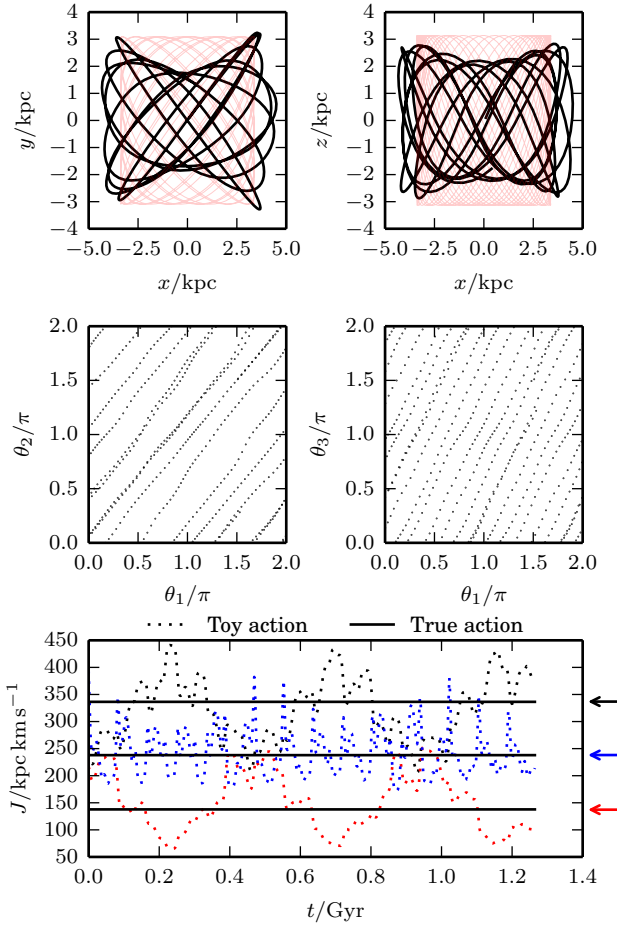


Figure 2. As Fig. 1 but for a box orbit.

For the loop orbit the true and recovered actions are

$$\begin{aligned} \mathbf{J}_{\text{true}} &= (212.09, 1307.54, 708.15) \text{kpc km s}^{-1} \\ \mathbf{J}_{\text{recov}} &= (213.33, 1307.29, 709.16) \text{kpc km s}^{-1}, \end{aligned}$$

and the true and recovered frequencies are

$$\begin{aligned} \boldsymbol{\Omega}_{\text{true}} &= (21.76474, 15.65172, 19.33786) \text{Gyr}^{-1} \\ \boldsymbol{\Omega}_{\text{recov}} &= (21.76508, 15.65185, 19.33780) \text{Gyr}^{-1}. \end{aligned}$$

In Fig. 3 we show two cross-sections of \mathbf{n} -space showing the absolute value of the components of the generating function. (For the isochrone potential we use the convention that subscript 1 refers to J_r , subscript 2 refers to L_z and subscript 3 refers to $J_z \equiv L - |L_z|$.) We see that the two most significant modes are $\mathbf{n} = (-1, 2, 0)$, which causes a mixing between the radial motion and azimuthal motion, and $\mathbf{n} = (0, 0, 2)$. Note that the S_n decrease towards the boundary so we are content that we have included the relevant modes.

For the box orbit the true and recovered actions are

$$\begin{aligned} \mathbf{J}_{\text{true}} &= (336.39, 137.78, 237.96) \text{kpc km s}^{-1} \\ \mathbf{J}_{\text{recov}} &= (336.85, 137.26, 238.17) \text{kpc km s}^{-1}, \end{aligned}$$

and the true and recovered frequencies are

$$\begin{aligned} \boldsymbol{\Omega}_{\text{true}} &= (39.752, 46.409, 73.814) \text{Gyr}^{-1} \\ \boldsymbol{\Omega}_{\text{recov}} &= (39.750, 46.406, 73.811) \text{Gyr}^{-1}. \end{aligned}$$

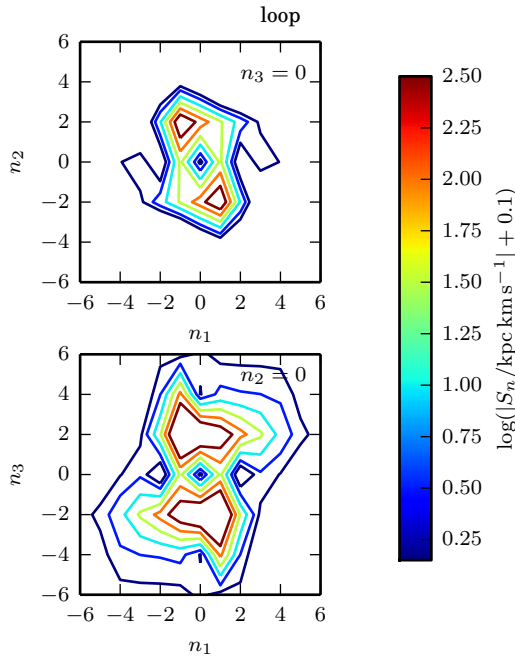


Figure 3. Cross-sections of the S_n as a function of \mathbf{n} for the loop orbit. In the top panel we show the cross-section $n_3 = 0$. The most significant mode in this plane is $(-1, 2, 0)$, which causes a mixing between the radial motion and azimuthal motion. In the lower plane we show the cross-section $n_2 = 0$, in which the mode $(0, 0, 2)$ is the most significant.

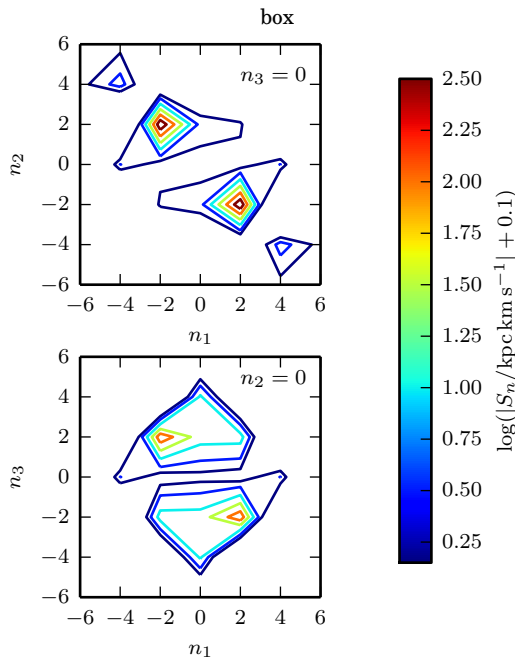


Figure 4. As Fig. 3 for the box orbit. The most significant mode in the plane $n_3 = 0$ (top) is $(2, -2, 0)$, which causes a mixing between the x motion and the y motion. In the plane $n_2 = 0$ the most significant mode is $(2, 0, -2)$.

In Fig. 4 we show two cross-sections of \mathbf{n} -space showing the absolute value of the components of the generating function. The two most significant modes are $\mathbf{n} = (2, -2, 0)$, which causes a mixing between the x motion and the y motion, and $\mathbf{n} = (2, 0, -2)$, which mixes the x and z motions. These modes are required to distort the rectangular orbits of the triaxial harmonic oscillator into those bounded by surfaces of constant confocal ellipsoidal coordinate. Note that the S_n decrease towards the boundaries as required. Also the structure of Fig. 3 is much richer than that of Fig. 4, signalling that the generating function has many more significant terms.

3.1 Accuracy of the method

Fig. 5 shows errors in J'_3 and Ω'_3 for the box orbit as a function of N_{\max} for various choices of the total integration time T . We have linked N_{\max} to N_T via equation (21). However we have not ensured that equations (19) and (20) are satisfied for each case. The weight of the points is proportional to the largest gap in coverage for the N modes. We see that in general a longer integration time provides a more accurate estimate of the action and particularly the frequency. We can understand this as a longer line segment provides a better measurement of the gradient for noisy data. From Fig. 5 we see that when working with high N_{\max} it is not sufficient to satisfy equation (21). We must also satisfy equation (20) such that we have a sufficient sampling in toy-angle space to constrain these higher modes.

For $T = 2T_F$ equation (20) is not satisfied for $N_{\max} \geq 4$. For large N_{\max} and $T = 2T_F$ many modes have insufficient coverage and the results are very poor. For the other three integration times equation (20) is not satisfied for $N_{\max} \geq 8$. For $T = 4T_F$ this results in an immediate deterioration of the frequency recovery as we have included a mode with $\max(\mathbf{n} \cdot \boldsymbol{\theta}) - \min(\mathbf{n} \cdot \boldsymbol{\theta}) \approx \pi/2$. For $T = 8T_F$ and $T = 12T_F$ a lack of coverage has not affected the results apart from for $T = 8T_F$ and $N_{\max} = 12$ where the frequency recovery is poorer. The mode which is not well covered is also not well covered for $N_{\max} = 8$ but we only see the effects of this lack of coverage when we try to include more modes. For $T = 12T_F$ both the action and frequency recovery are very good despite equation (20) not being satisfied when $N_{\max} \geq 8$. In particular there is one mode for which $\max(\mathbf{n} \cdot \boldsymbol{\theta}) - \min(\mathbf{n} \cdot \boldsymbol{\theta}) \approx 4.3$. It seems that this coverage is sufficient to not degrade the results. In conclusion, when equation (20) is satisfied we recover the frequencies and actions well, whilst when it is not satisfied the recovery deteriorates in some cases, particularly that of the frequency.

Finally, we find that when we double the number of time samples used for the examples shown in Fig. 5 the results change significantly only when equation (20) is not satisfied. Therefore, we conclude that provided we have more equations than unknowns and have satisfied equations (19) and (20) the actions and frequency recovery will be satisfactory.

3.2 Near-resonant orbit

To illustrate some of the points discussed we show results for a near-resonant orbit. This orbit is a box orbit with the initial conditions $(x, y, z) = (0.1, 0.1, 0.1)$ kpc, $(v_x, v_y, v_z) = (142, 150, 216.5)$ km s $^{-1}$. Again we integrate for time $T = 8T_F$ and set $N_{\max} = 6$. The results are shown in Fig. 6. The frequency vector of this orbit is nearly parallel to $\mathbf{n} = (-4, 0, 2)$ so the coverage of this mode is very poor and $\max(\mathbf{n} \cdot \boldsymbol{\theta}) - \min(\mathbf{n} \cdot \boldsymbol{\theta}) \approx 1.11$

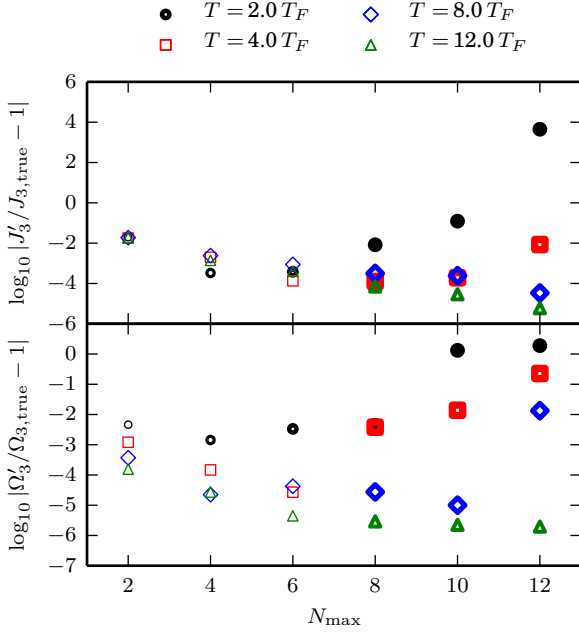


Figure 5. Error in the recovered values of J'_3 and Ω'_3 for the box orbit as a function of N_{\max} and the total integration time. We work with even multiples of the period, T_F , corresponding to the lowest frequency. The size of the points is proportional to the largest gap in coverage for the N modes. In general a longer integration time provides more accurate actions and frequencies. When attempting to constrain higher modes it is necessary to integrate the orbit for a longer period to ensure that the sampling in toy angle is sufficient.

for $\mathbf{n} = (-4, 0, 2)$. However, the true and recovered actions are

$$\mathbf{J}_{\text{true}} = (301.74, 147.63, 165.36) \text{ kpc km s}^{-1}$$

$$\mathbf{J}_{\text{recov}} = (300.69, 147.66, 165.89) \text{ kpc km s}^{-1},$$

and the true and recovered frequencies are

$$\mathbf{\Omega}_{\text{true}} = (43.318, 50.369, 86.724) \text{ Gyr}^{-1}$$

$$\mathbf{\Omega}_{\text{recov}} = (43.386, 50.371, 86.777) \text{ Gyr}^{-1}.$$

As seen before, poor coverage in one of the modes is not detrimental to the action and frequency recovery.

4 APPLICATION

As a brief application of the method outlined in this paper we will inspect the action diagram for a realistic triaxial Galactic potential. We take the potential from Law & Majewski (2010). This potential was found to produce the best fit to the Sagittarius stream data. This potential has three components: a disc defined by the Miyamoto-Nagai potential

$$\Phi_{\text{disc}}(x, y, z) = \frac{-GM_{\text{disc}}}{\sqrt{x^2 + y^2 + (a + \sqrt{z^2 + b^2})^2}}, \quad (24)$$

with $M_{\text{disc}} = 10^{11} M_{\odot}$, $a = 6.5 \text{ kpc}$ and $b = 0.26 \text{ kpc}$; a spherical bulge described by the Hernquist profile

$$\Phi_{\text{bulge}}(r) = \frac{-GM_{\text{bulge}}}{r + c}, \quad (25)$$

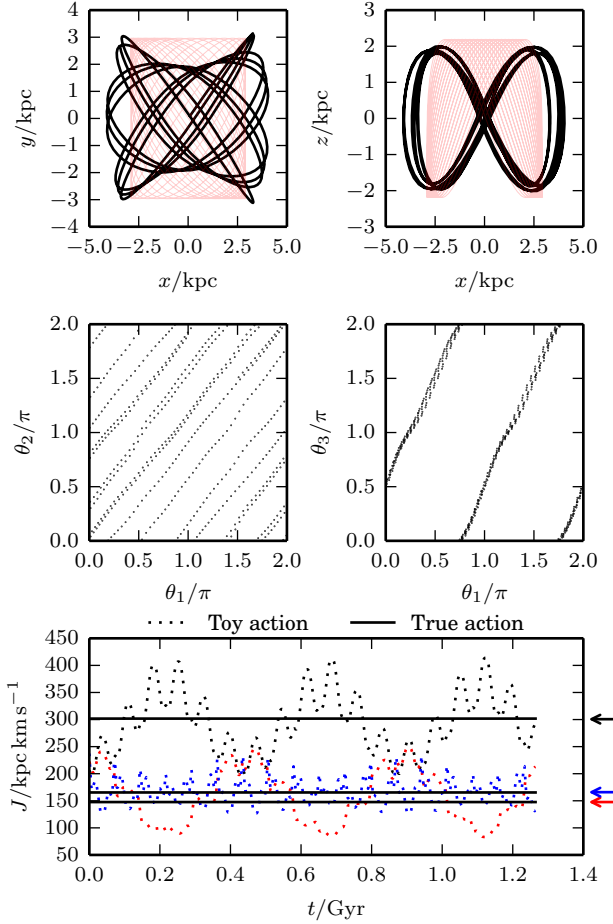


Figure 6. Example near-resonant orbit in the triaxial Stäckel potential – the top panels shows in black the orbit integrated in the test potential. This is a short-axis loop orbit so circulates about the axis $z = 0$. In faint red we show the initial point integrated in the best-fitting isochrone potential. In the middle panels we show the toy angles calculated at each time sample. In the bottom panel we show the toy actions at each time-step as a dotted line (black for J_1 , blue for J_2 and red for J_3). The solid lines show the true actions and the arrows mark the estimated actions.

with $M_{\text{bulge}} = 3.4 \times 10^{10} M_{\odot}$ and $c = 0.7 \text{ kpc}$; and the triaxial logarithmic halo

$$\Phi_{\text{halo}}(x, y, z) = v_{\text{halo}}^2 \log \left(C_1 x^2 + C_2 y^2 + C_3 xy + \frac{z^2}{q_z^2} + r_{\text{halo}}^2 \right) \quad (26)$$

with $v_{\text{halo}} = 121.7 \text{ km s}^{-1}$, $C_1 = 0.99 \text{ kpc}^{-2}$, $C_2 = 0.53 \text{ kpc}^{-2}$, $C_3 = 0.11 \text{ kpc}^{-2}$, $q_z = 1.36$ and $r_{\text{halo}} = 12 \text{ kpc}$.

4.1 An example orbit

We inspect a single orbit in this potential in Fig. 7. The chosen orbit is a short-axis loop orbit with initial condition $(x, y, z) = (14.69, 1.80, 0.12) \text{ kpc}$, $(v_x, v_y, v_z) = (15.97, -128.90, 44.68) \text{ km s}^{-1}$. We use different, but overlapping, $8T_F$ long segments of the orbit with $N_T = 500$ to calculate the actions, angles and frequencies using $N_{\max} = 6$. We ensure equation (20) is satisfied for these time samplings. This orbit lies in the surface of constant energy explored in the next section. We find

that the action and frequency are

$$\begin{aligned} \mathbf{J}' &\approx (160.18, 2186.16, 36.09) \text{ kpc km s}^{-1} \\ \Omega' &\approx (27.26, 19.12, 37.01) \text{ Gyr}^{-1}. \end{aligned}$$

The error in the actions and frequencies can be estimated by the spread of the estimates from each segment. We find

$$\begin{aligned} \Delta \mathbf{J}' &\approx (0.07, 0.08, 0.03) \text{ kpc km s}^{-1}, \\ \Delta \Omega' &\approx (3 \times 10^{-4}, 6 \times 10^{-5}, 2 \times 10^{-3}) \text{ Gyr}^{-1}. \end{aligned}$$

For each orbit segment we find $\theta'(0)$ and these different values should all lie along straight lines with gradients given by the derived frequencies. In Fig. 7 we show that the condition is well satisfied.

Using different orbit segments is perhaps the only way to estimate the error in an action or frequency found using the present method. It is simplest to use consecutive orbit segments as we have here. However, a better method is to use orbit segments separated by a large time interval. This can be achieved most effectively by utilizing the estimated generating function to find an initial condition for a second orbit integration. A simple choice is to increase one of the derived angle coordinates by $\pi/2$.

4.2 A typical constant energy surface

Now we turn to constructing the action diagram for the chosen potential. For a given energy (that of a particle dropped at 18 kpc on the intermediate axis) we launched particles at a series of points linearly spaced between 0.2 and 18 kpc along the potential's intermediate axis with the velocity vector perpendicular to the axis and inclined at linearly spaced angles to the z -axis between 0 and $\pi/2^1$. We integrated each initial condition for ~ 10 Gyr saving $N_T = 1000$ samples. For all orbits the energy was conserved to one part in 10^6 . We set $N_{\text{max}} = 6$ and ensured that equations (19) and (20) were satisfied. If equation (19) was not satisfied, we had undersampled the orbit, so we took a finer sampling. If equation (20) was not satisfied we did not have sufficient coverage, so we continued integrating for another 10 Gyr, taking another 1000 samples. We then calculated the actions from the time series. Fig. 8 shows each orbit as a point in 3D action-space². We see that the surface of constant energy is a triangle-shaped plane in action-space. The points are coloured based on their orbit classification. An equivalent figure for a Stäckel potential can be found in de Zeeuw (1985).

In a triaxial potential, the loop orbits can be divided into two classes: the short-axis loops that loop around the short axis (in our case the z -axis) and the long-axis loops that loop around the long axis (the x -axis). Along with the box orbits these three classes of orbit occupy distinct regions on the action-space plane of constant energy. At each corner of the plane only one action is non-zero and the corresponding orbit is the parent orbit of each of the three classes: the $J_2 = 0, J_3 = 0$ orbit is a radial orbit along the long

¹ Note that the intermediate axis of the halo model proposed by Law & Majewski is actually the z -axis. However, at small radii ($\lesssim 18$ kpc) the intermediate axis of the full potential is in the (x, y) plane due to the disc contribution, and the z -axis is the short axis.

² To produce a continuous plane in action-space we must scale the 'radial' actions of the loop orbits, J_1 , by a factor of 2. J_1 for a loop orbit corresponds to a single oscillation from minimum to maximum coordinate and back, whilst for a box orbit a single oscillation covers the interval 0 to maximum coordinate four times.

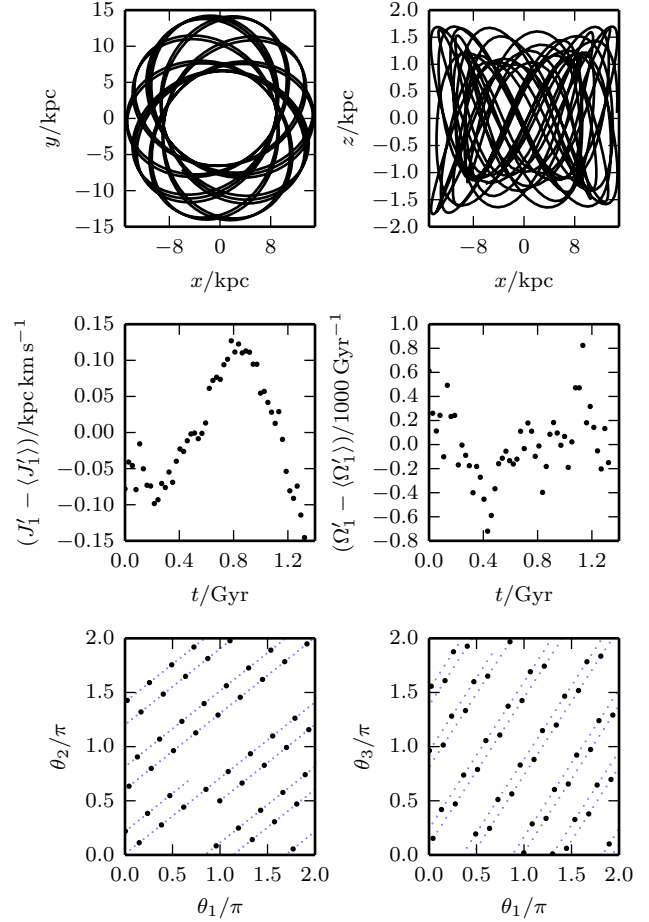


Figure 7. An example orbit in the Law & Majewski (2010) potential. It is a short-axis loop orbit with actions $\mathbf{J}' \approx (160, 2186, 36) \text{ kpc km s}^{-1}$. In the top panel we show a $16T_F$ long orbit segment in the (x, y) and (x, z) planes. In the central two panels we show the spread in J'_1 and Ω'_1 calculated using 500 time-samples from an $8T_F$ orbit segment labelled by its initial time sample. In the bottom panel we show the calculated angles at these times with black dots. We also show the angles found using $\theta'(0) + \Omega' t_i$ with one of the calculated frequencies and initial angles in smaller blue dots.

axis, the $J_1 = 0, J_3 = 0$ orbit is a closed orbit in the (x, y) plane and the $J_1 = 0, J_2 = 0$ orbit is a closed orbit in the (y, z) plane. We note that near the interface between the different orbit classes some regions of the plane are depleted of points (our choice of initial sampling causes an increased density of points near the edges of the plane). Also there is some overlap between the different orbit classes in the action space. These features are due to the presence of resonant islands with surrounding chaotic orbits at the interface of the regular orbit regions (see Section 5.3). For orbits near the box/loop boundary it can take many orbital periods to correctly identify the orbit class (Carpintero & Aguilar 1998), and some may be misclassified.

5 DISCUSSION

5.1 Relation to previous work

The problem addressed here goes back to Binney & Spergel (1982, 1984), who Fourier transformed the time series $x(t_i)$ of individual

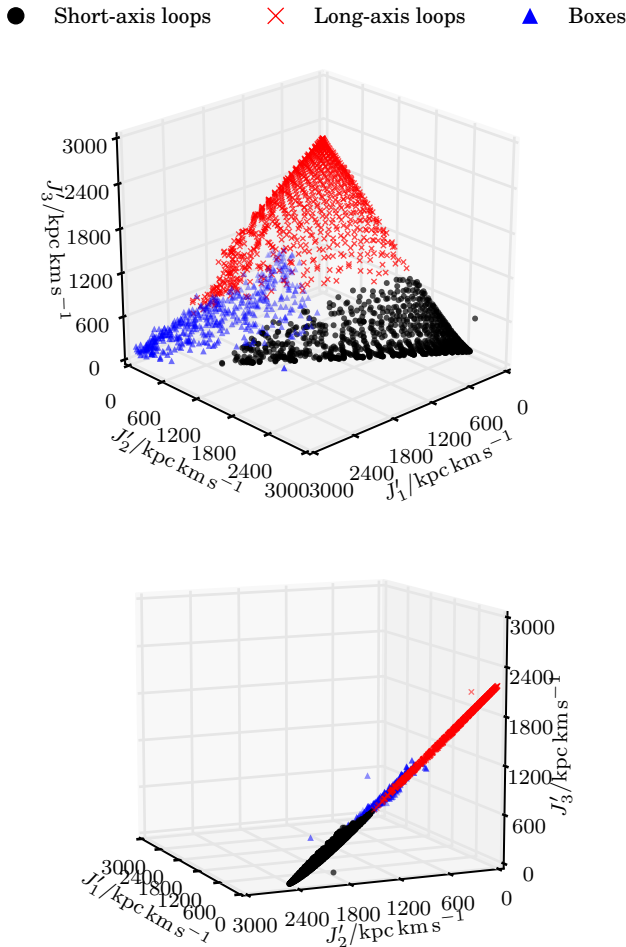


Figure 8. Two projections of a surface of constant energy in the 3D action space of the potential proposed by Law & Majewski (2010). Black circles show short-axis loop orbits, red crosses show long-axis loop orbits and blue triangles show box orbits.

coordinates and assigned to each line in the resulting spectrum appropriate integers n_j so that ωt could be identified with $\sum_j n_j \Omega_j t$. Once this identification had been successfully accomplished, $\Omega_j t$ could be replaced with θ_j to yield the orbit’s angle representation. This approach is inferior to that introduced here in several respects: (i) Whereas the generating function is a scalar, a star’s location is described by a vector, so it is wasteful to construct the angle representations of all three coordinates rather than the angle representation of the generating function: Binney & Spergel (1984) failed to take advantage of the strong restrictions on tori that arise from angle-action coordinates being canonical. (ii) It is not straightforward to measure correctly the complex amplitudes A from the discrete Fourier transform of a time series such as $x(t_i)$ because the required amplitude will in general not lie at one of the discrete frequencies sampled. (iii) When an orbit is near-resonant there is often dangerous ambiguity in the integers n_j that should be assigned to a particular line. With the present technique we work from the outset with periodic functions and their Fourier series so the issue of how frequencies fall on a discrete grid does not arise. Moreover, the assignment of integers n_j to Fourier terms is unambiguous.

The method described here has significant overlap with the work of Warnock (1991) on the construction of magnetic coordinates and the related method of Kaasalainen & Binney (1994) for

the construction of angle coordinates. In both these studies angle-action variables were evaluated along numerically computed orbits. The coordinates evaluated were not those of a toy potential but of a trial torus that had been previously constructed: Warnock (1991) was refining the Fourier coefficients S_n while Kaasalainen & Binney (1994) were solving for the $\partial_i S_n$ given the S_n . In both these studies, several initial conditions for orbit integration were chosen on each torus to overcome the problem that with a single short integration a resonant orbit yields a highly non-uniform distribution of sample points on the torus. Since we do not have a good representation of the target torus until the equations have been set up and solved, we cannot take advantage of this possibility.

Warnock (1991) solved for the discrete Fourier transforms of the nS_n rather than for the S_n because the matrix that then has to be inverted is nearly diagonal when the toy and target tori are close to one another and the sample points provide a nearly regular grid in the space of toy angles. Since our toy and target tori can be quite different, and it is hard to achieve a uniform sampling of toy-angle space, we have not used Warnock’s technique.

5.2 Possibility of using Stäckel tori

We have used completely different toy potentials for each class of orbit, and it is natural to ask whether it would not be advantageous to use always a Stäckel potential since such a potential has tori of every type. We have not pursued this option for two reasons. First, the actions and angles of Stäckel potentials require the evaluation of integrals whereas the potentials we have used yield algebraic expressions for angles and actions. Secondly, and more fundamentally, when integrating an orbit that lies close to the box/loop interface, it would be non-trivial to ensure that the toy torus with the actions of the target orbit had the same geometry as the target torus. By using potentials that support only one type of torus, we are assured from the outset that this condition is satisfied. However, this rests on our correct identification of the orbit type from the time series. As we saw with the Law & Majewski potential, in some marginal cases it may take many orbital periods to correctly identify the orbit.

5.3 Resonances and chaos

We have focused here on orbits that are non-resonant members of the major orbital families. In real galactic potentials one encounters orbits that are either resonantly trapped or chaotic (e.g. §3.7 Binney & Tremaine 2008). Chaotic orbits can be thought of as sequences of sections of resonantly trapped orbits, so these two types of orbit raise similar issues.

In a generic integrable potential, the frequencies Ω_i depend on the actions, so on some tori a resonant condition $\mathbf{n} \cdot \boldsymbol{\Omega} = 0$ is satisfied. Consequently, individual orbits on these resonant tori do not cover the entire torus since the condition $\mathbf{n} \cdot \boldsymbol{\theta} = \text{constant}$ constrains the angle variables. This lack of coverage makes it impossible to determine some of the Fourier coefficients S_n .

When the potential is strictly integrable, orbits on tori that are adjacent to a resonant torus completely cover their tori although they take a long time to do so. In a generic potential, however, such orbits move over a series of tori without covering any of them, as they librate around the strictly resonant orbit. Consequently, these orbits have some of the characteristics of a strictly resonant torus. When the present technique is used on a resonantly trapped orbit, the generating function will map the toy torus into a close approximation to the strictly resonant torus, so in an N -body model

the density of stars on this torus will seem to be larger than it really is. Hence with the present technique, resonantly trapped orbits will give rise to apparent crowding in action space that is analogous to the signature of resonances when particles are mapped into frequency space by determining orbital frequencies by Fourier decomposition of coordinates (Dumas & Laskar 1993): when the ratios Ω_2/Ω_1 and Ω_3/Ω_1 are used to place orbits in frequency-ratio space, the existence of resonantly trapped orbits leads to a crowding of points along the straight lines associated with certain resonance conditions $\mathbf{n} \cdot \boldsymbol{\theta} = \text{constant}$ (Binney & Tremaine 2008, §3.7.3(b)).

Chaotic orbits can be considered as moving through a series of quasi-periodic orbits. Therefore the recovered actions and frequencies from our method will be a function of the total integration time. We see that the region of the constant energy surface occupied by the box orbits in Fig. 8 has considerable crowding and the regular grid of initial conditions is not visible. This is indicative of chaotic orbits which have been allocated very different actions from one initial condition to the next.

In Fig. 9 we perform the same procedure as outlined in §3.7.3(b) of Binney & Tremaine (2008) to inspect the ratio of frequencies plane of a logarithmic potential. We use the potential

$$\Phi(\mathbf{x}) = \frac{1}{2} \log \left(x^2 + \frac{y^2}{q_y^2} + \frac{z^2}{q_z^2} + r_c^2 \right), \quad (27)$$

with $q_y = 0.9$, $q_z = 0.7$ and $r_c^2 = 0.1$. We drop a series of test particles on the surface $\Phi(\mathbf{x}) = 0.5$ regularly spaced in the spherical polar coordinates ϕ and $\cos \theta$, and integrate each initial condition for a time $T = 200$ extracting $N_T = 2048$ samples. We then use our method to find the corresponding orbital frequencies and plot their ratio in Fig. 9. As noted in Binney & Tremaine (2008) the top-right corner of this plane shows the regular spacing of the initial conditions whilst the lower-left corner shows a more irregular distribution with no evidence of the regular grid of initial conditions used to produce it. Also, we find that there are overdensities along lines corresponding to resonances. Our plot is very similar to that shown in Binney & Tremaine (2008). However, the structure of the irregular bottom-left region differs. This is to be expected as it is these orbits which are irregular, and how one assigns regular properties to them depends on the method employed.

6 CONCLUSIONS

We have presented a method for finding actions, frequencies and angles from numerically integrated orbits in a general potential³. The method relies on estimating the Fourier components of the generating function that maps a toy torus into the torus on which the computed orbit lies by solving systems of linear algebraic equations. This method enables one to determine the angle-action coordinates $(\boldsymbol{\theta}, \mathbf{J})$ of a given phase-space point (\mathbf{x}, \mathbf{v}) . It has numerous possible applications in astronomy.

Ours is the first method presented in the literature for finding the actions in a general triaxial potential. Triaxiality is an essential ingredient of dark-matter distributions, and a realistic Galactic model which should include non-axisymmetric features such as the bar, and the potentially triaxial halo. This method is a necessary first step towards constructing distribution functions, $f(\mathbf{J})$, for these more complex Galactic components.

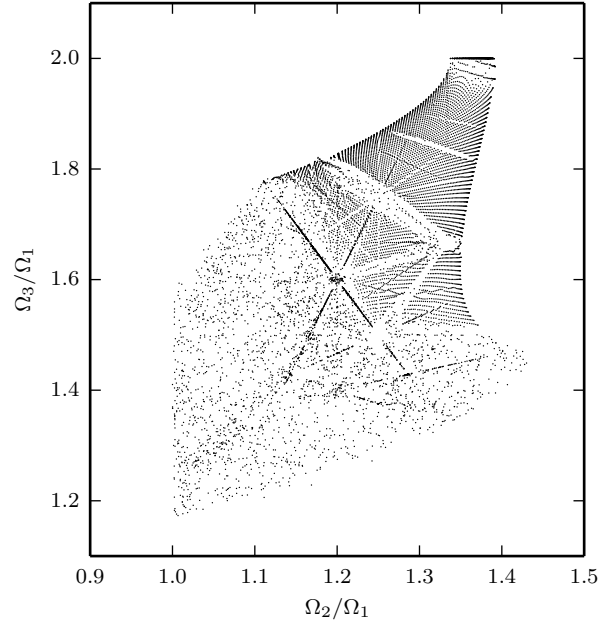


Figure 9. Frequency ratios in the triaxial logarithmic potential extracted from orbital time series using the method presented in this paper. Each point corresponds to an initial condition for a particle dropped on the surface $\Phi(\mathbf{x}) = 0.5$.

An important application is to the analysis of N -body simulations. A single N -body snapshot consists of 3D positions and velocities for $\sim 10^9$ particles. Letting the simulation evolve for a few time steps produces another snapshot with a completely different set of 10^9 positions and velocities. Thus the particles' phase-space coordinates constitute a highly degenerate and non-compact representation of the simulation. Effective analysis of the simulation should start by condensing the coordinates into a smaller set of numbers. This can be done by replacing the $6N_T$ numbers $(\mathbf{x}_i, \mathbf{v}_i)$ with just three numbers J_i and plotting each particle as a point in 3D action space. The simulation then becomes a density of particles in a 3D space. This representation will greatly facilitate the comparison of different N -body models. Also it may prove possible to find good fits to the star density in terms of analytic functions, as Pontzen & Governato (2013) have done for numerical dark-matter haloes and appears to be possible for the Galactic discs (Binney 2012b; Binney et al. 2014). We hope to report on an application of this method to an N -body simulation soon.

It should be noted that it is not advisable to take the N_T time samples of a given orbit directly from the simulation. Rather at some time t the potential should be computed on a spatial grid (e.g. Magorrian 2007), and the equations of motion in this potential should be integrated for N_T timesteps starting from the phase-space location of each particle at time t . These integrations in a fixed potential lend themselves to massive parallelization, for example on a Graphical Processor Unit (GPU) so it should be possible to compute angle-action coordinates for very large numbers of particles.

Here we discussed time-reversible triaxial potentials. In this case we can determine a priori the phases of the terms in the generating function. Rotation of the figure of the potential destroys the time-reversibility of the Hamiltonian and we lose the ability to set the phases a priori. In the worst case, the S_n in equation (5) become

³ We will make the code developed for this paper available at <https://github.com/jlsanders/genfunc>.

complex numbers that are only limited by the condition $S_{-n} = S_n^*$ required to make the generating function real. Extending the current framework to this case \sim doubles the dimensionality of the matrices we must solve for given N_{\max} .

ACKNOWLEDGEMENTS

JS acknowledges the support of STFC. JB was supported by STFC by grants R22138/GA001 and ST/K00106X/1. The research leading to these results has received funding from the European Research Council under the European Union's Seventh Framework Programme (FP7/2007-2013) / ERC grant agreement no. 321067.

REFERENCES

- Arnold V. I., 1978, *Mathematical methods of classical mechanics*. New York: Springer
- Binney J., 2012a, *MNRAS*, 426, 1324
- Binney J., 2012b, *MNRAS*, 426, 1328
- Binney J. et al., 2014, *MNRAS*, 439, 1231
- Binney J., Spergel D., 1982, *ApJ*, 252, 308
- Binney J., Spergel D., 1984, *MNRAS*, 206, 159
- Binney J., Tremaine S., 2008, *Galactic Dynamics: Second Edition*. Princeton University Press
- Carpintero D. D., Aguilar L. A., 1998, *MNRAS*, 298, 1
- de Zeeuw T., 1985, *MNRAS*, 216, 273
- Dumas H. S., Laskar J., 1993, *Physical Review Letters*, 70, 2975
- Kaasalainen M., Binney J., 1994, *MNRAS*, 268, 1033
- Law D. R., Majewski S. R., 2010, *ApJ*, 714, 229
- Magorrian J., 2007, *MNRAS*, 381, 1663
- Marvasti F., ed., 2001, *Nonuniform sampling. Theory and practice*. Dordrecht: Kluwer Academic/ Plenum Publishers, pp. xxvi + 924
- McGill C., Binney J., 1990, *MNRAS*, 244, 634
- McMillan P. J., 2013, *MNRAS*, 430, 3276
- McMillan P. J., Binney J. J., 2008, *MNRAS*, 390, 429
- Pontzen A., Governato F., 2013, *MNRAS*, 430, 121
- Press W. H., Teukolsky S. A., Vetterling W. T., Flannery B. P., 2002, *Numerical recipes in C++: the art of scientific computing*. Cambridge University Press
- Sanders J. L., Binney J., 2013, *MNRAS*, 433, 1826
- Schwarzschild M., 1979, *ApJ*, 232, 236
- Sellwood J. A., 2010, *MNRAS*, 409, 145
- Valluri M., Debattista V. P., Quinn T., Moore B., 2010, *MNRAS*, 403, 525
- Vera-Ciro C., Helmi A., 2013, *ApJL*, 773, L4
- Warnock R. L., 1991, *Physical Review Letters*, 66, 1803

APPENDIX A: SYMMETRIES

In Section 2.2 we asserted that for a time-reversible Hamiltonian the Fourier components of the generating function, S_n , are real. However, it must also be true that there is a point on the target torus where $\dot{\mathbf{J}} = \mathbf{0}$. McGill & Binney (1990) show that this is true if the toy potential is an isochrone and the target Hamiltonian is axisymmetric. Additionally they demonstrated that when the potential is symmetric about the plane $z = 0$, Fourier components of the generating function with odd n_z vanish. Here we repeat these arguments extended to the 3D triaxial case.

A1 Loop orbits

Let us first consider the loop orbits. Suppose we have a target Hamiltonian of the form

$$H(r, \phi, \vartheta) = \frac{1}{2}p_r^2 + \frac{p_\phi^2}{2r^2 \sin^2 \vartheta} + \frac{p_\vartheta^2}{2r^2} + \Phi(r, \phi, \vartheta), \quad (\text{A1})$$

where (r, ϕ, ϑ) are standard spherical polar coordinates. The equations of motion for the toy actions are

$$\begin{aligned} \dot{J}_i &= -\frac{\partial H}{\partial \theta_i} \\ &= \left(\frac{p_\vartheta^2}{r^3} + \frac{p_\phi^2}{r^3 \sin^2 \vartheta} - \frac{\partial \Phi}{\partial r} \right) \frac{\partial r}{\partial \theta_i} + \left(\frac{p_\phi^2 \cos \vartheta}{r^2 \sin^3 \vartheta} - \frac{\partial \Phi}{\partial \vartheta} \right) \frac{\partial \vartheta}{\partial \theta_i} \\ &\quad - \frac{\partial \Phi}{\partial \phi} \frac{\partial \phi}{\partial \theta_i} - p_r \frac{\partial p_r}{\partial \theta_i} - \frac{p_\vartheta}{r^2} \frac{\partial p_\vartheta}{\partial \theta_i} - \frac{p_\phi}{r^2 \sin^2 \vartheta} \frac{\partial p_\phi}{\partial \theta_i}. \end{aligned} \quad (\text{A2})$$

Now let us consider the point $\boldsymbol{\theta} = (0, 0, \pi/2)$: at this point the particle is at pericentre, at a maximum in its vertical oscillation and at $\phi = 0$. Therefore at this point we have that

$$\frac{\partial r}{\partial \theta_i} = \frac{\partial \vartheta}{\partial \theta_i} = p_r = p_\vartheta = \frac{\partial p_\phi}{\partial \theta_i} = 0, \quad (\text{A3})$$

so

$$\dot{J}_i = -\frac{\partial \Phi}{\partial \phi} \frac{\partial \phi}{\partial \theta_i}. \quad (\text{A4})$$

In a triaxial potential with its axes aligned with the coordinate axes, $x = 0$ is a symmetry plane of the potential so $\partial \Phi / \partial \phi|_{\phi=0} = 0$ and $\dot{J}_i = 0$. This is the requirement introduced in Section 2.2 for the Fourier components of the generating function to be real. Now let us consider the point $\boldsymbol{\theta} = (0, 0, 0)$. Here the particle is at pericentre, crossing the $z = 0$ plane, and at $\phi = 0$. At this point we have

$$\frac{\partial r}{\partial \theta_i} = \cos \vartheta = p_r = \frac{\partial p_\vartheta}{\partial \theta_i} = \frac{\partial p_\phi}{\partial \theta_i} = 0, \quad (\text{A5})$$

so

$$\dot{J}_i = -\frac{\partial \Phi}{\partial \phi} \frac{\partial \phi}{\partial \theta_i} - \frac{\partial \Phi}{\partial \vartheta} \frac{\partial \vartheta}{\partial \theta_i}. \quad (\text{A6})$$

As we saw before the first term is zero as $x = 0$ is a symmetry plane of the potential. The second term is also zero as $z = 0$ is also a symmetry plane. By a similar argument at $\boldsymbol{\theta} = (0, \pi/2, 0)$, $\partial \Phi / \partial \phi|_{\phi=\pi/2} = 0$ as $y = 0$ is a symmetry plane of the potential.

We calculate $\dot{\mathbf{J}}$ from equation (8) as

$$\dot{\mathbf{J}} = \sum_{n \in \mathbf{N}} 2n \left(\mathbf{i}n \cdot \dot{\boldsymbol{\theta}} \right) S_n(\mathbf{J}') \sin n \cdot \boldsymbol{\theta} \quad (\text{A7})$$

At the point $\boldsymbol{\theta} = (0, 0, \pi/2)$ we know $\dot{\mathbf{J}} = \mathbf{0}$ so we require $\sin \pi n_3 / 2 = 0$ so n_3 must be even. Similarly we know $\dot{\mathbf{J}} = \mathbf{0}$ at $\boldsymbol{\theta} = (0, \pi/2, 0)$ so n_2 is restricted to even values. However, n_1 can take any integer value.

A2 Box orbits

Now let us consider the box orbits. We have a target Hamiltonian of the form

$$H = \frac{1}{2} \sum_i p_i^2 + \Phi(x, y, z) \quad (\text{A8})$$

where $p_i = (p_x, p_y, p_z)$ and the equations of motion for the toy actions are

$$\dot{J}_i = -\sum_j \frac{\partial \Phi}{\partial x_j} \frac{\partial x_j}{\partial \theta_i} - p_j \frac{\partial p_j}{\partial \theta_i} \quad (\text{A9})$$

Consider the point $\boldsymbol{\theta} = (0, 0, 0)$. Here the orbit is turning in all three coordinates so $\mathbf{p} = \mathbf{0}$ and $\partial\mathbf{x}/\partial\theta_i = \mathbf{0}$ so $\dot{\mathbf{J}} = \mathbf{0}$ as required in Section 2.2. Now let us consider the point $\boldsymbol{\theta} = (\pi/2, 0, 0)$. Here the orbit is turning in y and z and is passing through the $x = 0$ plane at which point $\partial p_x/\partial\theta_i = 0$ as p_x is at a maximum. Therefore we have

$$\dot{J}_i = -\frac{\partial\Phi}{\partial x} \frac{\partial x}{\partial\theta_i}. \quad (\text{A10})$$

For a triaxial potential aligned with our choice of Cartesian axes $x = 0$ is a symmetry plane so $\partial\Phi/\partial x|_{x=0} = 0$. Therefore $\dot{\mathbf{J}} = \mathbf{0}$ here and by similar arguments to the loop orbit case we are restricted to even n_1 . We can employ the same arguments by considering the stationary points $\boldsymbol{\theta} = (0, \pi/2, 0)$ and $\boldsymbol{\theta} = (0, 0, \pi/2)$ to show that n_2 and n_3 must be even.

APPENDIX B: ANGLES AND FREQUENCIES

To find the angles and frequencies from an orbit timeseries we must minimize equation (16) with respect to the unknowns. The unknowns are $\boldsymbol{\theta}'(0)$, $\boldsymbol{\Omega}'$ and the set of $\partial S_n/\partial\mathbf{J}'$, which we denote as $(\partial_1 S_n, \partial_2 S_n, \partial_3 S_n)$. For each time we define the N -vector

$$\mathbf{s}_n(t_i) = -2 \sin(\mathbf{n} \cdot \boldsymbol{\theta}(t_i)). \quad (\text{B1})$$

We also define the $3(2 + N)$ -vectors

$$\mathbf{x}_\theta \equiv (\boldsymbol{\theta}'(0), \boldsymbol{\Omega}', \partial_1 S_n, \partial_2 S_n, \partial_3 S_n), \quad (\text{B2})$$

$$\mathbf{b}_\theta \equiv \sum_i (\boldsymbol{\theta}(t_i), t_i \boldsymbol{\theta}(t_i), \theta_1(t_i) \mathbf{s}(t_i), \theta_2(t_i) \mathbf{s}(t_i), \theta_3(t_i) \mathbf{s}(t_i)) \quad (\text{B3})$$

and the symmetric matrix

$$\mathbf{A}_\theta \equiv \sum_i \begin{pmatrix} \mathbf{I}_3 & t_i \mathbf{I}_3 & \mathbf{s}^{1\text{T}} & \mathbf{s}^{2\text{T}} & \mathbf{s}^{3\text{T}} \\ t_i \mathbf{I}_3 & t_i^2 \mathbf{I}_3 & t_i \mathbf{s}^{1\text{T}} & t_i \mathbf{s}^{2\text{T}} & t_i \mathbf{s}^{3\text{T}} \\ \mathbf{s}^1 & t_i \mathbf{s}^1 & \mathbf{s} \cdot \mathbf{s}^{\text{T}} & 0 & 0 \\ \mathbf{s}^2 & t_i \mathbf{s}^2 & 0 & \mathbf{s} \cdot \mathbf{s}^{\text{T}} & 0 \\ \mathbf{s}^3 & t_i \mathbf{s}^3 & 0 & 0 & \mathbf{s} \cdot \mathbf{s}^{\text{T}} \end{pmatrix}, \quad (\text{B4})$$

where each \mathbf{s}^m is an N -by-3 matrix with the N -vector \mathbf{s} in the m th column, and each \mathbf{s} is evaluated at the i th time. Setting the partial derivatives of F with respect to the unknowns to zero yields the matrix equation,

$$\mathbf{A}_\theta \cdot \mathbf{x}_\theta = \mathbf{b}_\theta. \quad (\text{B5})$$

This paper has been typeset from a $\text{\TeX}/\text{\LaTeX}$ file prepared by the author.